

# Quality control for more reliable integration of deep learning-based image segmentation into medical workflows

Elena Williams<sup>1,2,7</sup>, Sebastian Niehaus<sup>1,3,4,7\*</sup>, Janis Reinelt<sup>1</sup>, Alberto Merola<sup>1</sup>, Paul Glad Mihai<sup>1</sup>, Ingo Roeder<sup>3,5</sup>, Nico Scherf<sup>3,4,6</sup>, Maria del C. Valdés Hernández<sup>2</sup>

1 – AICURA medical, Bessemerstrasse 22, 12103 Berlin, Germany.

2 – Centre for Clinical Brain Sciences. University of Edinburgh.

3 – Institute for Medical Informatics and Biometry, Carl Gustav Carus Faculty of Medicine, Technische Universität Dresden, Fetscherstrasse 74, 01307 Dresden, Germany.

4 – Max Planck Institute for Human Cognitive and Brain Sciences, Stephanstrasse 1a, 04103 Leipzig, Germany.

5 - National Center of Tumor Diseases (NCT) Partner Site Dresden, Fetscherstrasse 74, 01307 Dresden, Germany

6 Center for Scalable Data Analytics and Artificial Intelligence ScaDS.AI, Dresden/Leipzig, Germany, 04103 Leipzig, Germany

7- These authors contributed equally: Elena Williams and Sebastian Niehaus.

\*Contact: niehaus@cbs.mpg.de

## Abstract

Machine learning algorithms underpin modern diagnostic-aiding software, which has proved valuable in clinical practice, particularly in radiology. However, inaccuracies, mainly due to the limited availability of clinical samples for training these algorithms, hamper their wider applicability, acceptance, and recognition amongst clinicians. We present an analysis of state-of-the-art automatic quality control (QC) approaches that can be implemented within these algorithms to estimate the certainty of their outputs. We validated the most promising approaches on a brain image segmentation task identifying white matter hyperintensities (WMH) in magnetic resonance imaging data. WMH are a correlate of small vessel disease common in mid-to-late adulthood and are particularly challenging to segment due to their varied size, and distributional patterns. Our results show that the aggregation of uncertainty and Dice prediction were most effective in failure detection for this task. Both methods independently improved mean Dice from 0.82 to 0.84. Our work reveals how QC methods can help to detect failed segmentation cases and therefore make automatic segmentation more reliable and suitable for clinical practice.

## Introduction

Medical image segmentation is essential for clinical decision-making and treatment planning. However, manual assessment of medical images, incorporated in nationwide medical-support systems is time-consuming and can lead to inaccurate results impacting clinical decisions. Despite Convolutional Neural Networks (CNN) being able to already perform image segmentation tasks with accuracies equaling or surpassing those of humans [1], inaccuracies cannot be completely avoided, which can lead to reduced acceptance by clinicians. Thus, it is important to understand the constraints and instabilities of a CNN model and assess the quality of the reported results (e.g., identify failed segmentation cases where the predicted output was wrong or inaccurate) making it safer and more reliable. As manual quality control on a large scale is not attainable, automated methods are being developed.

In medical image segmentation, the most common quality control (QC) approaches used to detect failed results include i) estimation and visualisation of uncertainty and errors [2]–[9], ii) aggregation of the uncertainty and error estimates into a single score [2], [3], [7], [10]–[14], and iii) prediction of quality class or Dice coefficient, a measure commonly used to assess the spatial agreement between the ground truth and the predicted segmentation map [7], [15]–[20].

The architecture of standard CNN models does not allow uncertainty estimation for predicting their output [21]. The most common method to address this issue is to use the Monte Carlo (MC) dropout in the hidden layers of the neural network [5]–[7], [9], [14], [15], [21], [22] which will allow approximation of the Bayesian inference. To extract the uncertainty, the model with MC dropout layers samples  $N$  predictions for every input. The final prediction is estimated by averaging the  $N$  prediction maps. Then, using various measures such as entropy and predictive variance [3]–[5], [14], [15], [23], the voxel-wise uncertainty levels are extracted from the final prediction map. Other eminent methods for capturing uncertainty include test-time augmentation [3], [7], [8], [24], network ensembles [2], [25], combination of the CNN model with the conditional variational autoencoder [26], and application of the “shadowed sets” theory [27], [28]. Error estimates can be obtained with the application of generative models which aim to approximate the model distribution to the true data distribution for generating new samples with some variations. Automatic QC can be also

implemented using error segmentation maps [12], [16], [19], [29]. Error maps are usually calculated by subtracting voxels of generated images or segmentation maps from the voxels of original input samples. It is assumed that if the segmentation output is not optimal, an obvious difference between the generated sample and the input sample would be apparent [19], [29].

Uncertainty and error maps can be used for visual assessment or correction of segmentation results [2], [12]. They can also be used to train a regression or classification model to predict Dice coefficients that could potentially substitute true Dice values [7], [15], [20]. The linear relationship between predicted Dice and true Dice can be evaluated by calculating the Pearson correlation coefficient or drawing scatter plots. It is assumed that the more linear the relationship, the more likely the predictive measure will successfully substitute Dice values. Two studies reported the highest correlation being achieved using the reverse classification accuracy (RCA) algorithm [17], [18]. However, a study aimed to segment skin lesions [15] reported the RCA to perform worse than a CNN regression model. The study noted that the RCA works well only in cases where objects to be segmented have a similar shape and location such as body organs. Results from uncertainty and error maps can be represented by a single score that can be used for failure detection in cases where it has a strong linear relationship with Dice values. This score can comprise measures like the intersection over union overlap [14], quality metric [12], [13], mean voxel-wise uncertainty [7], [14] and the pixel-wise sum [10], [11].

The main contribution of this work is the application and evaluation of state-of-the-art automatic QC methods to detect failed segmentation results. We apply the QC methods to a challenging and clinically relevant brain imaging segmentation task. Our work contributes to facilitating the further implementation and integration of these methods in clinical practice. We further demonstrate the advantages and disadvantages of each method when applied to a common task and provide recommendations for QC method selection. By providing an overview of the performance of these QC methods in a highly heterogeneous sample in terms of image acquisition protocols and patients' health conditions, this study intends to assist researchers in developing robust medical image segmentation pipelines by guiding the selection of the QC strategy. We illustrate the necessity of the

use of quality control methods as a key step for the optimal interaction between physicians and machine learning systems.

The relevance of these QC methods increases with unknown data sets since it is not feasible to determine and describe what the application domain for the CNN model is. These unknown environments are encountered in decentralized training environments such as those found in federated learning [30] or swarm learning [31]. Decentralized training environments are becoming increasingly important in medicine as they allow large medical training datasets to be used without clinical sites having to share the data or information about the data [32].

## Results

In this work, we implemented four state-of-the-art QC approaches for CNN-based segmentation models to evaluate their applicability and practical value in one of the most widely researched tasks in medical image analysis: the segmentation of white matter hyperintensities (WMH) from structural magnetic resonance imaging (MRI) scans. We used MRI data from various publicly available data sets acquired in different centers. The approaches evaluated in this work are uncertainty and error map estimation, aggregation of the maps into a single score, and prediction of Dice values. To estimate the uncertainty, we implemented Kayalibay U-net [33] and added MC dropout in the hidden layers of the model, the uncertainty maps were obtained with an application of entropy measure on the predicted segmentation maps. The MC U-net model was evaluated using Dice measure which estimates an overlap between the ground truth and predicted segmentation map, the formula is given in Methods section. To evaluate the QC performance of error estimates, Kayalibay U-net was adjusted to perform a reconstruction task, the error maps were estimated by subtracting the reconstructed MRI images from the real ones. The reconstruction U-net was evaluated using structural similarity index measure (SSIM). The aggregation was performed using voxel-wise sum operation (VS) over uncertainty and error maps. To predict the Dice values, we implemented a CNN Regression model and ran experiments with various inputs. We evaluated how well these QC methods perform in detecting failures in the identification and boundary delineation of WMH qualitatively and using statistical measures, such as correlation coefficient, mean absolute error,

Precision and Recall. Further details on metrics, network architectures and training procedures are given in Methods section and Supplementary Material, part D.

### *Visualization of uncertainty and error estimates*

Examples of estimated uncertainty and error maps for brains with different WMH burden are shown in Figure 1. Consistent with findings from state-of-the-art methods applied to the same task in different cohorts (reviewed in [34]), sometimes our models under-segmented small WMH (see (a), Prediction Map) as well as large WMH (c), while showing high accuracy segmenting WMH in brains with medium WMH load (b). Uncertainty was mostly located on the borders of the WMH regions and larger differences were found more on the error maps for brains with large WMH burden (c). High uncertainty levels were also detected in areas where artefacts were mistakenly classed as WMH in the ground truth and, therefore, present in the ground truth map (see (c), Uncertainty Map), but, correctly, not misclassified as WMH in the prediction map. Although the reconstructed images look almost identical to the true images, there are prediction errors, particularly in the WMH regions, displayed by the error maps as intensity differences.

In our test sample the MC U-net achieved an average Dice score of 0.819 whereas the reconstruction (Rec) U-net reached an average structural similarity index measure (SSIM) coefficient of 0.933, both across a 5-fold cross-validation. There was no observed difference between the folds. Hence, the visualisations of uncertainty and error maps (Figure 1) as well as the scatter plots (Figures 2 and 3) are provided with respect to only one of the folds, i.e. fold 1.

### *Aggregation of uncertainty and error estimates*

The scatter plots in Figure 2 demonstrate that the values of the voxel-wise sum (VS) extracted from the uncertainty maps and the respective Dice coefficients are relatively linearly distributed in contrast to the aggregated error estimates, which exhibit larger confidence intervals. The numeric results of the VS performance are summarised in Table 1. The Pearson correlation coefficient

between the uncertainty VS and Dice was 0.55 ( $P < 0.05$ ). No significant correlation was observed between Dice and error VS values ( $r -0.32, P > 0.1$ ).

We removed the samples with an uncertainty VS lower than 1100 as these instances also had low Dice coefficients (Figure 2, a). After the removal of failed segmentation maps, the mean Dice value increased from 0.819 to 0.833 by detecting 3 failed cases on average with Precision of 0.94 and Recall of 1. Using a threshold error VS value of -100,000, which correlated with the Dice value of one of the observations with lowest Dice (Figure 2, b), we identified two poorly segmented samples, which were responsible for the drop in mean Dice value from 0.819 to 0.817, with Precision of 0.89 and Recall of 0.81. The performance per fold is shown in Supplementary Materials, part C.

### *CNN Regression*

Table 1 shows that the Dice predictions with uncertainty-prediction input produced the lowest mean absolute error (MAE 0.045) and highest correlation coefficient ( $r 0.71, P < 0.0001$ ) showing a strong and positive relationship between the predicted and true Dice. The highest MAE was achieved with the error-prediction input and the lowest correlation coefficient with the image-prediction pair.

Figure 3 shows three scatter plots with predicted and true Dice values from one of the folds. Dice values predicted with image-prediction and uncertainty-prediction pairs were higher than the true Dice values. However, Dice values predicted with error-prediction pairs were slightly lower than the true Dice values. The observations on the scatter plots (b, c) were located closer to the regression line and had narrower confidence intervals.

The QC performance obtained from removing results with predicted Dice values lower than 0.75 is shown in Table 1. The reported number of segmentation results removed (N) was calculated as an average across 5-folds. Dice values predicted with an input of error-prediction pairs allowed us to

identify the highest number of failed segmentations (c) and produced the highest increase in the median Dice value, namely from 0.819 to 0.833, with Precision of 0.941 and Recall of 0.833. The results per fold are shown in Supplementary Materials, part C.

## Discussion

The safety of the application of machine learning models is crucial for its successful adoption in clinical practice. In this study, we evaluated state-of-the-art QC methods which aimed at detecting failed CNN-based WMH segmentation results. The estimation of correlation coefficients, precision and recall allowed us to successfully compare the performance of the QC methods. We show how QC methods can detect failed cases making automatic segmentation more reliable and suitable for clinical routines. The validation results presented highlight how machine learning algorithms can be integrated using QC techniques and offer the prospect of obtaining the required medical product certification for application of these algorithms in real clinical scenarios.

The most popular QC approaches identified in the literature are visualisation of uncertainty and error estimates, aggregation of the estimates into a single score, and prediction of Dice coefficients. The implementation of these techniques showed that the aggregation of uncertainty estimates and Dice prediction were the most effective methods in identifying failed cases. Among these, Dice prediction yielded the most encouraging results for automatic QC. From our experiments, we saw the highest number of detected failed cases and an improved mean Dice value using a model trained with a combination of error and prediction maps.

The aggregation of error maps was inadequate in failure detection, as we did not find a relationship between the segmentation quality and aggregated error estimates. We found, however, uncertainty maps to be effective in identifying failed segmentation results when estimates were aggregated in a single score. We demonstrated that failed cases can be identified by using a voxel-wise sum operation over an uncertainty map. Similar to what was reported in [20], we observed high levels of uncertainty to be mostly present on the borders of WMH regions and rarely on the missing areas or false positive areas. This makes the application of uncertainty maps for visual assessment or correction of WMH segmentation output ineffective, as its results can be misleading. For this reason, we cannot recommend the application of uncertainty maps of the purpose of visual QC in clinical practice. Though we used a similar uncertainty measure as in [4], we cannot compare our visual



results because unlike the original study we did not aggregate voxel-wise uncertainty into structure-wise regions.

Similar to what is reported in [10], [11], we found a significant correlation between the VS values and Dice coefficients. We also saw an improved mean Dice value after we removed failed segmentation maps based on VS values. This supports our hypothesis that VS values extracted from uncertainty maps can be used as a substitute for Dice coefficients in cases when the ground truth is not available. We assumed the same would be true with aggregated error maps. However, the VS measure did not show any significant correlation with Dice values and we had to reject our null hypothesis.

In the experiments with Dice prediction, we achieved a similar performance to the one demonstrated in [15], [16], [20], [29]. Unlike the other works, we validated not only the model performance but also the efficacy of Dice prediction in failure detection. We ran the experiments using three input types to see which features would work best in identifying failed segmentation results. We note that, although an input of uncertainty and prediction maps showed the highest correlation and the lowest error with true Dice values, it was moderately effective for automatic QC. The best QC performance was demonstrated using Dice coefficients predicted with an error-prediction pair. This can be attributed to the fact that the model trained with an input of error-prediction pair slightly under-predicted the Dice values whereas the models trained with image-prediction and uncertainty-prediction pairs slightly over-predicted the Dice values.

The main strength of this study is the evaluation of the effectiveness of QC methods in detecting inaccurate segmentations. For every QC approach we performed detection of unsuccessful segmentation maps and evaluated it using 5-fold cross-validation, based on which we show how successful the method was in identifying failed cases. None of the published studies i) compared mean Dice values before and after detection of unsuccessful segmentation results, ii) analysed the number of failed cases identified and iii) estimated Precision and Recall coefficients to show how well the proposed QC approach performed in practice. Usually only the error rate or correlation

coefficient between the predicted and true measure of segmentation quality as well as qualitative assessment had been reported. This information is not enough to evaluate the efficacy of an automatic QC system. Additionally, we quantitatively analysed state-of-the-art QC methods. From the literature review performed, we note that automatic QC for medical image segmentation has become an actively developing field of research in the last three years. However, very few papers so far attempted to summarise the latest findings and evaluate the performance of state-of-the-art QC methods in practice [2], [15], [20].

In addition to the strengths mentioned above, our work has also limitations. Firstly, as was reported in [4], there is a statistically significant correlation between the WMH burden and segmentation quality measured e.g. in Dice values. This might not be the case for other segmentation applications targeted at areas that are more consistent in size and location, such as other body organs and some types of tumors. This implies that although QC approaches showed good performance on WMH, they may not generalise well on other input data. Further validation of QC methods using a different type of image data and segmentation problem such as cardiac MRI or liver CT scans segmentation is therefore needed.

## Methods

### *Materials*

We combined data from four databases of brain magnetic resonance images (MRI) from patients with white matter hyperintensities (WMH) of cardiovascular and Multiple Sclerosis (MS) origins, as they have a similar appearance [34]. By combining data from different sources, we ensured variations in the training sample to overcome overfitting problems common when a single imaging dataset is used [36]. The datasets used in this project were:

1. The dataset from the MICCAI WMH Challenge (MICCAI17) [37].
2. Data from the MS Lesion Segmentation Challenge at ISBI 2015 (MS15) collected from five patients at different time points [38]. Only data from one time point was used in the experiments to prevent overfitting.
3. The dataset from MICCAI MS segmentation challenge 2016 (MS16) [39].
4. The MR image database of MS pathology (MS17) [40].

Details on these datasets are shown in Table 3. In our experiments we used the ground truth segmentation maps as well as the T1-weighted and fluid attenuation inversion recovery (FLAIR) MRI sequences, which show different contrasts between tissue types. The T1-weighted MRI sequence offers a good contrast between the healthy brain tissues while FLAIR helps to distinguish pathologies present in white matter [41]. In total, there were T1-weighted and FLAIR MRI data samples from 105 patients. All experiments were run using 5-fold cross-validation. The data samples were randomly assigned to each fold and split into training, validation and test sets with a size of 68, 16, and 21, respectively. The details on data preprocessing are presented in Supplementary Materials parts B and C.

### *QC methods*

Using the results of a literature review we selected automatic QC approaches which are the most suitable for a CNN-based WMH segmentation task. The details on the literature review process are given in Supplementary Materials, part A. We implement and evaluate the performance of selected

QC methods such as visualisation of uncertainty and error estimates, aggregation of the estimates into a single score as well as prediction of Dice coefficients.

### *Monte Carlo U-net*

To implement a segmentation model, we chose the three-dimensional (3D) U-net architecture proposed by Kayalibay et al. [42] as it allows combining multiple segmentation maps on different scales. As Figure 4 shows, to allow uncertainty estimation, MC dropout layers were added after every convolutional block with a rate of 0.2 as in [14], [21], [43].

We used data augmentation methods to increase the sample size, cover a broader range of variations of the image appearances, and prevent overfitting. We applied noise and affine transformations of random varying amplitudes to the existent images and fed them to the training routine in each iteration. Image preprocessing included linear normalisation of voxel intensities in a range [0, 255], cropping the non-brain background to reduce sparsity, and reshaping to a uniform size of 128x128x128 voxels.

To train the MC U-net we used a combination of T1-weighted and FLAIR volumes. Further training parameters are described in the Supplementary Materials, at section D.B. For the gradient descent optimisation we used the Dice loss function (*Eq. 1*), where a minimum value of 0 indicates a perfect overlap between the ground truth and predicted segmentation map. Given the two segmentation maps for input  $i$ , namely original  $y_i$  and predicted  $\hat{y}_i$ , the Dice loss was calculated using the following formula:

$$Dice\ loss_{\hat{y}_i y_i} = 1 - \frac{2 \times |y_i \cap \hat{y}_i|}{|y_i| + |\hat{y}_i|} \quad Eq. 1$$

To obtain final prediction maps and extract the uncertainty, we passed forward the MC U-net model 20 times for every input;  $N = 20$  was chosen as it was shown to capture well the uncertainty levels [6], [15]. The average map  $\hat{y}_{i,avg}$  was calculated out of the 20 prediction maps as per *Eq. 2*:

$$\hat{y}_{i,avg} = \frac{1}{N} \sum_{N=1}^N \hat{y}_{i,n} \quad Eq. 2$$

To estimate uncertainty, we chose an entropy measure that previously has shown to capture well the modelling uncertainty for MS lesion segmentation outputs [4]. The entropy measure allows us to assess the amount of information inherent to the model’s predictive density function at every voxel. Using the base-2 logarithm of the average map  $\hat{y}_{i,avg}$ , the uncertainty map  $\tilde{H}_{\hat{y}_{i,avg}}$  is calculated, then, as follows:

$$\tilde{H}_{\hat{y}_{i,avg}} = -\hat{y}_{i,avg} \log_2 \hat{y}_{i,avg} - (1 - \hat{y}_{i,avg}) \log_2 (1 - \hat{y}_{i,avg}) \quad Eq. 3$$

### *Reconstruction U-net*

To estimate the error maps, we decided to implement a reconstruction (Rec) U-net as in [16]. We decided not to use conditional GANs (cGANs), because these require a multi-class segmentation map [12], [19], [29], whereas in the case of WMH segmentation only binary maps are used.

As shown in Figure 4, to create a reconstruction U-net we simply changed the last layer of the baseline U-net architecture with a ReLU activation function [44]. We used the FLAIR modality as input due to its characteristic of highlighting the white matter pathology. Similar as [16], for the training we inserted zeroes in 3D FLAIR images in the areas where the ground truth WMH segmentation regions were located for the network to learn recovering the missed areas. As shown in Eq. 4, the error maps  $EM_i$  were estimated by calculating the difference between the original images  $I_i$  and the reconstructed images  $\hat{I}_i$ :

$$EM_i = I_i - \hat{I}_i \quad Eq. 4$$

To train the reconstruction model, we used the structural similarity index measure (SSIM). The SSIM metric is calculated by estimating, for every original image  $y_i$  and reconstructed image  $\hat{y}_i$ , i) the mean voxel value ( $\mu_{y_i}, \mu_{\hat{y}_i}$ ) and ii) standard deviation ( $\sigma_{y_i}, \sigma_{\hat{y}_i}$ ) in order to compute and compare luminance  $l$ , contrast  $c$  and structures  $s$  as in Eq. 5-7 given below:

$$l_{\hat{y}_i y_i} = \frac{2\mu_{\hat{y}_i} \mu_{y_i} + c_1}{\mu_{\hat{y}_i}^2 + \mu_{y_i}^2 + c_1}, \text{ where } c_1 = L \times 0.01 \quad \text{Eq. 5}$$

$$c_{\hat{y}_i y_i} = \frac{2\sigma_{\hat{y}_i y_i} + c_2}{\sigma_{\hat{y}_i}^2 + \sigma_{y_i}^2 + c_2}, \text{ where } c_2 = L \times 0.03 \quad \text{Eq. 6}$$

$$s_{\hat{y}_i y_i} = \frac{\sigma_{\hat{y}_i y_i} + c_3}{\sigma_{\hat{y}_i} \sigma_{y_i} + c_3}, \text{ where } c_3 = c_2/2 \quad \text{Eq. 7}$$

The SSIM loss is then estimated using the Eq. 8:

$$SSIM \text{ loss}_{\hat{y}_i y_i} = 1 - (l_{\hat{y}_i y_i} \times c_{\hat{y}_i y_i} \times s_{\hat{y}_i y_i}) \quad \text{Eq. 8}$$

The SSIM measure was adjusted to estimate similarity with the maximum value of  $L = 1$ . Further implementation details are given in Supplementary Materials, section D.C.

### *CNN Regression*

As per the literature review, another common QC approach is to train a regression model to predict Dice values. To evaluate this approach, we built a 3D CNN Regression model, namely Reg-net. The model architecture is shown in Figure 4.

To compare which features are better at predicting the quality, we carried out three experiments using the following inputs:

1. Image-prediction pair  $(I_i, \hat{y}_{i,avg})$ .
2. Uncertainty-prediction pair  $(\tilde{H}_{\hat{y}_{i,avg}}, \hat{y}_{i,avg})$ .
3. Error-prediction pair  $(EM_i, \hat{y}_{i,avg})$ .

For every data sample in the training, validation and test sets across the 5-folds, we saved the average prediction maps  $\hat{y}_{i,avg}$  estimated using an MC U-net, its respective Dice scores, the uncertainty maps, and error maps. For the estimation of the error maps in this experiment, instead of

the ground truth segmentation maps, we used average prediction maps  $\hat{y}_{i,avg}$  to place 0s into the original FLAIR images. Further training parameters are given in the Supplementary Materials, at section D.E.

To optimise the Adam gradient descent algorithm, we used the Huber loss function. As demonstrated in Eq. 9, the Huber loss function utilises the parameter  $\delta$  which measures the spread between the observed and predicted values. Depending on the value of  $\delta$ , the loss can be estimated as i) the squared difference between the observed and predicted values and divided by two or ii) by estimating the difference between the absolute error multiplied by the parameter  $\delta$  and value of  $\delta$  divided by two:

$$Huber\ loss_{\hat{y}_i, y_i} = \begin{cases} \frac{1}{2}(y_i - \hat{y}_i)^2 & \text{for } |y_i - \hat{y}_i| \leq \delta \\ \delta|y_i - \hat{y}_i| - \frac{1}{2}\delta & \text{otherwise.} \end{cases} \quad Eq. 9$$

### *Statistical Analysis*

To evaluate the performance of QC approaches such as aggregation and Dice prediction, we used statistical metrics. Similar as in [10], [11], to aggregate uncertainty and error maps we used a voxel-wise sum (VS) measure. As demonstrated in [4], [45], small isolated WMH clusters are more difficult to estimate correctly. Therefore, it is often the case that WMH are poorly segmented in brain images with only small punctate clusters, manifesting in lower Dice values. Considering that uncertainty and error estimates are often based around the WMH regions [20], [29], we would expect that patient image data with a small WMH load would have lower VS coefficients. Consequently, our hypothesis is that small VS values would correlate with low Dice values. The more correlated the values, the more likely the proposed method can be used to estimate the quality in situations where the ground truth is not available and real Dice values cannot be obtained. To test this hypothesis, we estimated the Pearson correlation coefficient between the real Dice and VS values.

The minimum and maximum VS value depends on the voxel value range and the size of the volume: the bigger the volume size, the more voxels there will be in the uncertainty and error maps and the

higher the VS can get. *Eq. 10* shows an example of how the  $VS_i$  values were calculated using uncertainty maps  $\tilde{H}_{\hat{y}_i,avg,v}$ , where  $v$  is a voxel:

$$VS_i = \sum_{v=0}^V \tilde{H}_{\hat{y}_i,avg,v} \quad Eq. 10$$

In addition, to evaluate whether the aggregation of estimates can be used as a QC approach we set a threshold value which correlated with failed segmentation results and removed samples with VS value lower than it. This allows us to identify failed cases which should be passed down to the expert for manual delineation. Afterwards, we compared the mean Dice of segmentation results before and after removal. We also estimated the number of observations removed as well as Precision and Recall measures to see how effective the method was in failure detection (Supplementary Materials, at section D.E.). We considered the prediction maps with a Dice value of less than 0.75 to be poor quality and using this threshold we converted the sets of Dice values and VS values into boolean vectors.

In all experiments with Reg-net, the QC performance results were assessed using a mean absolute error (MAE) and Pearson correlation coefficient estimated between the true and predicted Dice. To evaluate whether the predicted Dice can be used for a QC purpose, we removed samples with the predicted Dice lower than 0.75. We also estimated the number of observations removed as well as Precision and Recall.

The analyses were performed using Python programming language. The network architecture and modelling process were implemented using Keras with a TensorFlow backend [46]. The training was run on a CPU-GPU hybrid system utilising 2 NVIDIA Tesla V100 GPUs (16 GB each) to parallelise the computation.



## References

- [1] R. A. Rava *et al.*, “Assessment of an Artificial Intelligence Algorithm for Detection of Intracranial Hemorrhage,” *World Neurosurgery*, vol. 150, pp. e209–e217, Jun. 2021, doi: 10.1016/J.WNEU.2021.02.134.
- [2] A. Jungo, F. Balsiger, and M. Reyes, “Analyzing the Quality and Challenges of Uncertainty Estimations for Brain Tumor Segmentation,” *Frontiers in Neuroscience*, vol. 14, Apr. 2020, doi: 10.3389/fnins.2020.00282.
- [3] G. Wang, W. Li, M. Aertsen, J. Deprest, S. Ourselin, and T. Vercauteren, “Aleatoric uncertainty estimation with test-time augmentation for medical image segmentation with convolutional neural networks,” *Neurocomputing*, vol. 338, pp. 34–45, Apr. 2019, doi: 10.1016/j.neucom.2019.01.103.
- [4] T. Nair, D. Precup, D. L. Arnold, and T. Arbel, “Exploring uncertainty measures in deep networks for Multiple sclerosis lesion detection and segmentation,” *Medical Image Analysis*, vol. 59, Jan. 2020, doi: 10.1016/j.media.2019.101557.
- [5] Y. Kwon, J. H. Won, B. J. Kim, and M. C. Paik, “Uncertainty quantification using Bayesian neural networks in classification: Application to biomedical image segmentation,” *Computational Statistics and Data Analysis*, vol. 142, Feb. 2020, doi: 10.1016/j.csda.2019.106816.
- [6] Z. Eaton-Rosen, F. Bragman, S. Bisdas, S. Ourselin, and M. J. Cardoso, “Towards safe deep learning: accurately quantifying biomarker uncertainty in neural network predictions,” Jun. 2018, [Online]. Available: <http://arxiv.org/abs/1806.08640>
- [7] H. Pan, Y. Feng, Q. Chen, C. Meyer, and X. Feng, *Prostate Segmentation From 3D Mri Using A Two-Stage Model and Variable-Input Based Uncertainty Measure*, 2019 IEEE 16th. International Symposium on Biomedical Imaging (ISBI), 2019. doi: 10.1109/ISBI.2019.8759300.
- [8] A. Norouzi, A. Emami, K. Najarian, N. Karimi, S. samavi, and S. M. R. Soroushmehr, “Exploiting Uncertainty of Deep Neural Networks for Improving Segmentation Accuracy in MRI Images,” in *ICASSP 2019 - 2019 IEEE International Conference on Acoustics, Speech and Signal Processing (ICASSP)*, 2019, pp. 2322–2326. doi: 10.1109/ICASSP.2019.8682530.
- [9] S. Hu, D. Worrall, S. Knecht, B. Veeling, H. Huisman, and M. Welling, “Supervised Uncertainty Quantification for Segmentation with Multiple Annotations,” in *Medical Image Computing and Computer Assisted Intervention – MICCAI 2019*, 2019, pp. 137–145.
- [10] H. P. Do, Y. Guo, A. J. Yoon, and K. S. Nayak, “Accuracy, uncertainty, and adaptability of automatic myocardial ASL segmentation using deep CNN,” *Magnetic Resonance in Medicine*, vol. 83, no. 5, pp. 1863–1874, May 2020, doi: 10.1002/mrm.28043.
- [11] Y. C. Kim, K. R. Kim, and Y. H. Choe, “Automatic myocardial segmentation in dynamic contrast enhanced perfusion MRI using Monte Carlo dropout in an encoder-decoder convolutional neural network,” *Computer Methods and Programs in Biomedicine*, vol. 185, Mar. 2020, doi: 10.1016/j.cmpb.2019.105150.
- [12] Z. Zhang, C. Tian, J. Li, Z. Zhong, Z. Jiao, and X. Gao, “Collaborative Boundary-aware Context Encoding Networks for Error Map Prediction,” 2020.
- [13] R. Zhang and A. C. S. Chung, “A Fine-Grain Error Map Prediction and Segmentation Quality Assessment Framework for Whole-Heart Segmentation,” in *Medical Image Computing and Computer Assisted Intervention*, 2019, pp. 550–558.
- [14] A. Guha Roy, S. Conjeti, N. Navab, and C. Wachinger, “Bayesian QuickNAT: Model uncertainty in deep whole-brain segmentation for structure-wise quality control,” *NeuroImage*, vol. 195, Mar. 2019, doi: 10.1016/j.neuroimage.2019.03.042.
- [15] T. DeVries and G. W. Taylor, “Leveraging Uncertainty Estimates for Predicting Segmentation Quality,” Jul. 2018, [Online]. Available: <http://arxiv.org/abs/1807.00502>
- [16] L. Zhou, W. Deng, and X. Wu, “Robust Image Segmentation Quality Assessment,” Mar. 2019, [Online]. Available: <http://arxiv.org/abs/1903.08773>
- [17] V. v. Valindria *et al.*, “Reverse Classification Accuracy: Predicting Segmentation Performance in the Absence of Ground Truth,” *IEEE Transactions on Medical Imaging*, vol. 36, no. 8, pp. 1597–1606, Aug. 2017, doi: 10.1109/TMI.2017.2665165.
- [18] R. Robinson *et al.*, “Automated quality control in image segmentation: Application to the UK Biobank cardiovascular magnetic resonance imaging study,” *Journal of Cardiovascular Magnetic Resonance*, vol. 21, no. 1, Mar. 2019, doi: 10.1186/s12968-019-0523-x.
- [19] I. Brusini *et al.*, “A deep learning-based pipeline for error detection and quality control of brain MRI segmentation results,” May 2020, [Online]. Available: <http://arxiv.org/abs/2005.13987>

- [20] F. Liu, Y. Xia, D. Yang, A. Yuille, and D. Xu, “An Alarm System for Segmentation Algorithm Based on Shape Model,” in *2019 IEEE/CVF International Conference on Computer Vision (ICCV)*, 2019, pp. 10651–10660. doi: 10.1109/ICCV.2019.01075.
- [21] Y. Gal and Z. Ghahramani, “Dropout as a Bayesian Approximation: Representing Model Uncertainty in Deep Learning,” in *Proceedings of the 33rd International Conference on International Conference on Machine Learning - Volume 48*, 2016, pp. 1050–1059.
- [22] A. Jungo, R. Meier, E. Ermis, E. Herrmann, and M. Reyes, “Uncertainty-driven Sanity Check: Application to Postoperative Brain Tumor Cavity Segmentation,” Jun. 2018, [Online]. Available: <http://arxiv.org/abs/1806.03106>
- [23] J. Sander, B. D. de Vos, J. M. Wolterink, and I. Išgum, “Towards increased trustworthiness of deep learning segmentation methods on cardiac MRI,” Mar. 2019, p. 44. doi: 10.1117/12.2511699.
- [24] M. Seçkin Ayhan and P. Berens, “Test-time Data Augmentation for Estimation of Heteroscedastic Aleatoric Uncertainty in Deep Neural Networks,” 2018.
- [25] B. Lakshminarayanan, A. Pritzel, and C. Blundell, “Simple and Scalable Predictive Uncertainty Estimation Using Deep Ensembles,” in *Proceedings of the 31st International Conference on Neural Information Processing Systems*, 2017, pp. 6405–6416.
- [26] C. F. Baumgartner *et al.*, “PHiSeg: Capturing Uncertainty in Medical Image Segmentation,” in *Medical Image Computing and Computer Assisted Intervention – MICCAI 2019*, 2019, pp. 119–127. doi: 10.1007/978-3-030-32245-8\_14.
- [27] H. Zheng *et al.*, “Deep pancreas segmentation with uncertain regions of shadowed sets,” *Magnetic Resonance Imaging*, vol. 68, pp. 45–52, May 2020, doi: 10.1016/j.mri.2020.01.008.
- [28] W. Pedrycz, “Shadowed sets: representing and processing fuzzy sets,” *IEEE Transactions on Systems, Man, and Cybernetics, Part B (Cybernetics)*, vol. 28, no. 1, pp. 103–109, 1998, doi: 10.1109/3477.658584.
- [29] Y. Xia, Y. Zhang, F. Liu, W. Shen, and A. L. Yuille, “Synthesize Then Compare: Detecting Failures and Anomalies for Semantic Segmentation,” in *Computer Vision – ECCV 2020*, 2020, pp. 145–161.
- [30] M. J. Sheller *et al.*, “Federated learning in medicine: facilitating multi-institutional collaborations without sharing patient data,” *Scientific Reports*, vol. 10, no. 1, p. 12598, 2020, doi: 10.1038/s41598-020-69250-1.
- [31] S. Warnat-Herresthal *et al.*, “Swarm Learning for decentralized and confidential clinical machine learning,” *Nature*, vol. 594, no. 7862, pp. 265–270, 2021, doi: 10.1038/s41586-021-03583-3.
- [32] N. Rieke *et al.*, “The future of digital health with federated learning,” *npj Digital Medicine*, vol. 3, no. 1, p. 119, 2020, doi: 10.1038/s41746-020-00323-1.
- [33] B. Kayalibay, G. Jensen, and P. van der Smagt, “CNN-based Segmentation of Medical Imaging Data,” Jan. 2017, [Online]. Available: <http://arxiv.org/abs/1701.03056>
- [34] R. Balakrishnan, M. del C. Valdés Hernández, and A. J. Farrall, “Automatic segmentation of white matter hyperintensities from brain magnetic resonance images in the era of deep learning and big data – A systematic review,” *Computerized Medical Imaging and Graphics*, vol. 88, p. 101867, Mar. 2021, doi: 10.1016/J.COMPAMEDIMAG.2021.101867.
- [35] M. Kabkab, E. Hand, and R. Chellappa, “On the size of Convolutional Neural Networks and generalization performance,” in *2016 23rd International Conference on Pattern Recognition (ICPR)*, 2016, pp. 3572–3577. doi: 10.1109/ICPR.2016.7900188.
- [36] H. Kuijf *et al.*, “Standardized Assessment of Automatic Segmentation of White Matter Hyperintensities and Results of the WMH Segmentation Challenge,” *IEEE Transactions on Medical Imaging*, vol. 38, pp. 2556–2568, 2019.
- [37] A. Carass *et al.*, “Longitudinal multiple sclerosis lesion segmentation: Resource and challenge,” *NeuroImage*, vol. 148, pp. 77–102, Mar. 2017, doi: 10.1016/j.neuroimage.2016.12.064.
- [38] O. Commowick *et al.*, “Objective Evaluation of Multiple Sclerosis Lesion Segmentation using a Data Management and Processing Infrastructure,” *Scientific Reports*, vol. 8, no. 1, Dec. 2018, doi: 10.1038/s41598-018-31911-7.
- [39] Ž. Lesjak *et al.*, “A Novel Public MR Image Dataset of Multiple Sclerosis Patients With Lesion Segmentations Based on Multi-rater Consensus,” *Neuroinformatics*, vol. 16, no. 1, pp. 51–63, Jan. 2018, doi: 10.1007/s12021-017-9348-7.
- [40] H. Li *et al.*, “Fully convolutional network ensembles for white matter hyperintensities segmentation in MR images,” *NeuroImage*, vol. 183, pp. 650–665, Dec. 2018, doi: 10.1016/J.NEUROIMAGE.2018.07.005.
- [41] P. Natekar, A. Kori, and G. Krishnamurthi, “Demystifying Brain Tumor Segmentation Networks: Interpretability and Uncertainty Analysis,” *Frontiers in Computational Neuroscience*, vol. 14, Feb. 2020, doi: 10.3389/fncom.2020.00006.

- [42] L. Gan and K. Zhang, “Image Super-Resolution Reconstruction Based on Deep Residual Network,” in *2020 IEEE International Conference on Artificial Intelligence and Computer Applications (ICAICA)*, 2020, pp. 359–364. doi: 10.1109/ICAICA50127.2020.9182694.
- [43] M. F. Rachmadi, M. del C. Valdés-Hernández, M. L. F. Agan, and T. Komura, “Deep learning vs. conventional machine learning: Pilot study of WMH segmentation in brain MRI with absence or mild vascular pathology,” *Journal of Imaging*, vol. 3, no. 4, Dec. 2017, doi: 10.3390/jimaging3040066.
- [44] F. Chollet and others, “Keras.” 2015.
- [45] A. Liberati *et al.*, “The PRISMA statement for reporting systematic reviews and meta-analyses of studies that evaluate healthcare interventions: explanation and elaboration,” *BMJ*, vol. 339, 2009, doi: 10.1136/bmj.b2700.
- [46] S. Smith, “Fast robust automated brain extraction,” *Human brain mapping*, vol. 17, pp. 143–155, Aug. 2002, doi: 10.1002/hbm.10062.

## Acknowledgments

### Funding:

MVH is supported by Row Fogo Charitable Trust (grant no. BRO-D.FID3668413)

### Author contributions:

Conceptualization: EW, SN, JR

Methodology: EW, SN, AM

Investigation: EW, SN, PGM

Visualization: EW

Supervision: NS, MVH, IR

Writing—original draft: EW, SN

Writing—review & editing: EW, SN, MVH, JR, AM, PGM, NS, IR

### Competing interests:

All authors declare they have no competing interests.

**Data and materials availability:** The full scripts and experiments are publicly available at [https://github.com/sebnieh/QA\\_for\\_WhiteMatterLesionSegmentation](https://github.com/sebnieh/QA_for_WhiteMatterLesionSegmentation). All data used are publicly available at the cited references.

## Figures and Tables

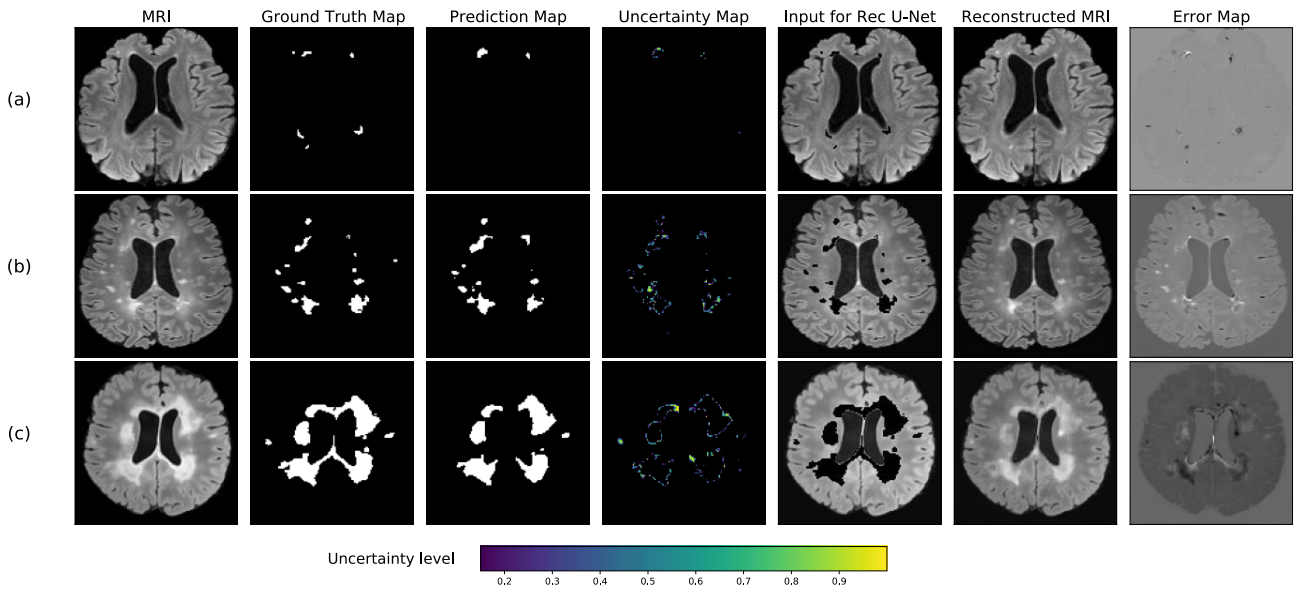


**Fig. 1.** The figure provides examples of T1-weighted brain MRI, segmentation ground truth map, prediction map, uncertainty map, input for Rec U-net model, prediction of Rec U-net and resulted difference, namely error map. The examples are given for MRI volumes with (a) small WMH, (b) medium WMH and (c) large WMH load. We note that the model sometimes under-segments in (a) as well as the in (c). We also see that the uncertainty is mostly located on the borders of the WMH regions and that the difference is more present on the error maps for large WMH.

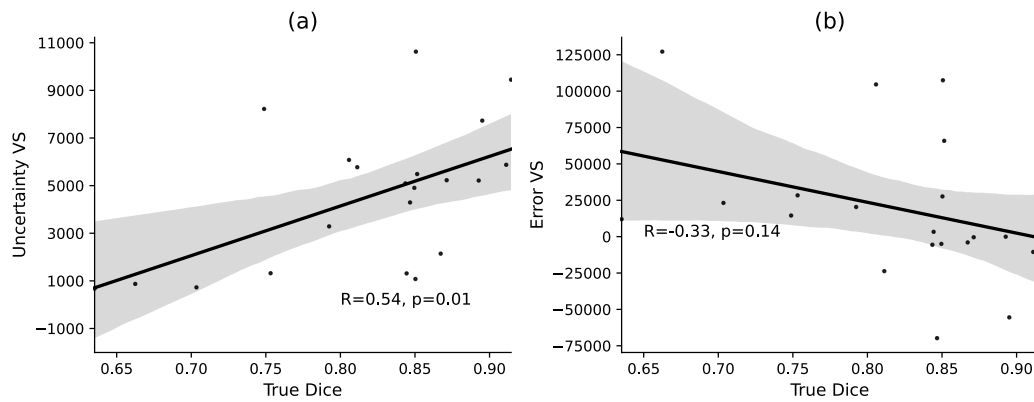


**Fig. 2.** Scatterplots of true Dice values and aggregated VS values from (a) uncertainty and (b) error maps with a regression line. We can see in (a) a linear positive relationship between the values of uncertainty VS and Dice. In (b), we note that the correlation is insignificant ( $R=-0.33$ ,  $p < 0.14$ ).

**Table 1.** QC performance results of VS aggregation and CNN regression experiments with different input data. Median results reported. MEDIAN Dice BEFORE removing failed segmentation results: 0.84

Analysis	VS Aggregation Performance		CNN Regression Performance		
	Uncertainty	Error	Image - Prediction	Uncertainty - Prediction	Error - Prediction
Correlation coefficient	0.52	-0.2517	0.566	0.7108	0.7329
Dice after filtering	0.85	0.838	0.8197	0.8191	0.838

<i>Precision</i>	0.929	0.477	0.8947	1.0 (4 folds 1, 1 fold 0.8421)	0.9412
<i>Recall</i>	0.89	0.829	0.8095	0.8095	0.8333
<i>N failed segmentations identified</i>	3.2	10.0	2.0	0.0	3.0
<i>MAE</i>	-	-	0.0536	0.045	0.0569

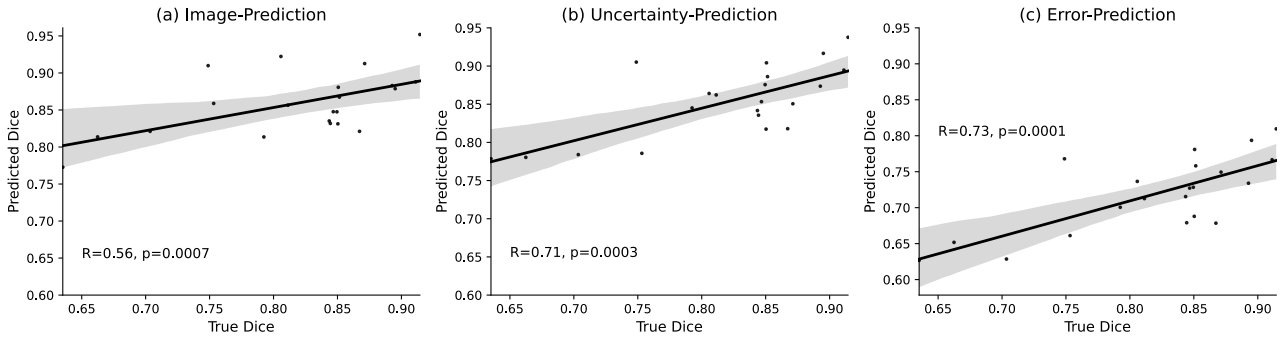


**Fig. 3.** Scatter plots of true Dice and predicted Dice with three input pairs, namely (a) image-prediction pair, (b) uncertainty-prediction pair and (c) error-prediction pair. In (c), we note that the predicted Dice values are slightly more correlated with true Dice values than in (a-b).

**Table 3.** Characteristics of the MR image databases used in the experiments.

Dataset	Location	Scanner Name	Voxel Size (mm <sup>3</sup> ) of T1 & FLAIR	Size of T1 & FLAIR Scans	Sample Size	Demographics	
						Male to female ratio	Age
MICCAI17	The Netherlands	3T Philips Achieva	0.96×0.95×3.00 T1 & FLAIR	240×240×48	20	Not given	Not given
	Singapore	3T Siemens TrioTim	1.00×1.00×3.00 T1 & FLAIR	232×256×48	20		
	The Netherlands	3T GE Signa HDxt	0.98×0.98×1.20 T1 & FLAIR	132×256×83	20		
MS15	The Netherlands	3T Philips Tesla	1.00×1.00×1.00 T1 & FLAIR	181×217×181	5	0.25	43.5±10.3
MS16	France	3T Philips Ingenia	0.74×0.74×0.85 T1w 0.74×0.74×0.7 FLAIR	336×336×261	5	0.87	45.5 ± 7.8
		3T Siemens Verio	1×1×1 T1w 0.5×0.5×0.11 FLAIR	256×256×176 T1w 512×512×144 FLAIR	5	0.36	43.6±12.6
MS17	Slovenia	3T Siemens Magnetom Trio	0.42×0.42×3.30 T1w 0.47×0.47×0.80 FLAIR	192×512×512	30	0.31	Median: 39.1

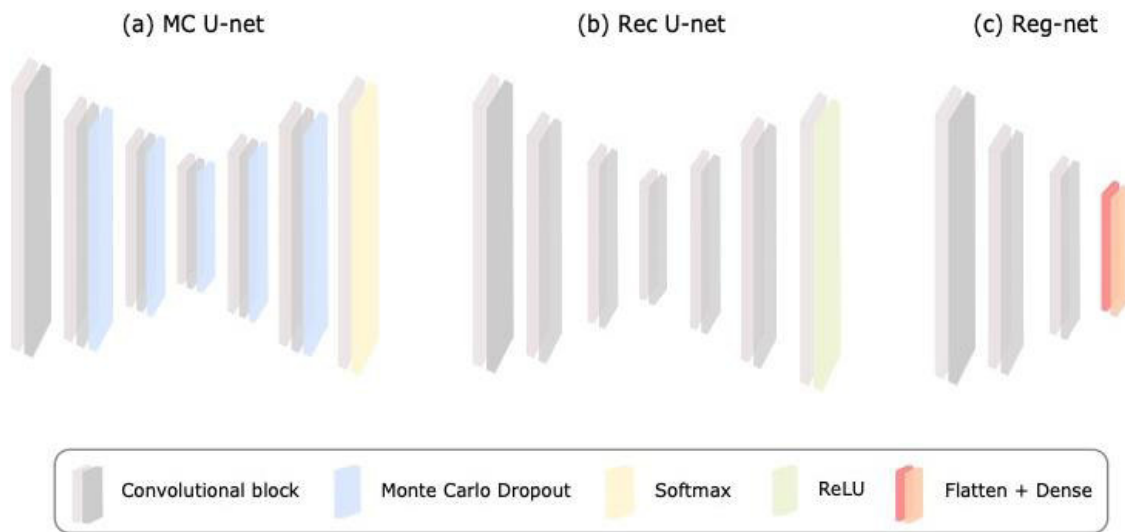


**Fig. 4.** The figure illustrates the architecture of 3 networks used in the experiments: (a) MC U-net, (b) Rec-net and (c) Reg-net. In (a) we can see an illustration of modified Kayalibay U-net architecture with MC dropout layers. In (b) the Kayalibay U-net architecture was adjusted for a reconstruction task. In (c) we present the architecture of 3D CNN regression, namely Reg-net, with features of size 16, 32, 64, 128 and linear activation function in the final Dense layer.

## Supplementary Materials

### A Literature review

#### A.A Protocol

We reviewed the literature following the recommendations given in the PRISMA statement [47]. A review protocol was developed to set out the main components and objectives of the review, search strategies, screening process and evidence synthesis. We defined the components of PICO principle which stands for Population, Intervention, Comparison and Outcome as follows:

- Population denotes adults with present brain lesions on MRI scans.
- The Intervention of interest represents quality control methods which are aimed at evaluating medical image segmentation.
- Comparison would include analysis of quality control implementations.
- The Outcome would be evidence of whether quality control methods improve the applicability of CNN-based white matter hyperintensities segmentation model.

The objectives of the review, were:

1. How successful was the quality control method in identifying failed segmentation results? What was the accuracy and how it was measured?
2. What are the main approaches used in implementation of the quality control methods for medical image segmentation? In particular, which algorithm was used for quality control of the segmentation?

### Search Strategies

The following databases were searched using keywords and in a free-text form: Web of Science and Google Scholar.

We selected studies published in English, from 2012 to the date(s) of the search.

Keywords included “CNN”, “deep learning”, “quality control”, “segmentation”, “quality assurance”, “uncertainty”, “white matter hyperintensities”, “brain lesions”, “MRI lesions”, “white matter lesions”, “WMH”, “MS lesions”, “instabilities” and “bias reduction”.

### Selection process

Studies were selected if they implemented quality control methods for automated lesion segmentation. Duplicated studies were removed. After screening titles and abstracts, we downloaded the full text of articles which meet the inclusion criteria and screened them again. The information on excluded studies and the reasons for exclusion were recorded and later presented in the standard PRISMA flow diagram which documents the screening process.

### Data Extraction

For each reviewed paper we extracted information regarding the dataset (e.g. size, pathologies, MRI sequences), segmentation method (e.g. CNN or a traditional supervised method, performance results), and quality control method (e.g. approach, accuracy).

### Synthesis

The narrative synthesis of the findings and its applicability were also extracted.

## **A.C Search results**

The search was conducted in the first week of September 2020. The Web of Science search resulted in 635 papers. After removing 6 duplicated studies, we screened the retrieved

abstracts and selected 35 papers. After further screening, only 21 of them were identified as falling within the inclusion criteria. The reasons for exclusion were recorded in the data extraction form. Further analyses of the full text resulted in 14 relevant studies being identified from the Web of Science. Similar search in Google Scholar yielded 3 more papers. Additionally, 7 studies were identified from screening the references of the studies previously identified. There was only 1 paper found on the topic of error maps through Google Scholar searches. Looking through the studies citing this 1 paper we found 4 more papers on the topic of error maps. As a result, there were 29 papers selected for the literature review. The PRISMA flow diagram was used to record the screening process. Out of 643 studies, 29 were selected for the review.

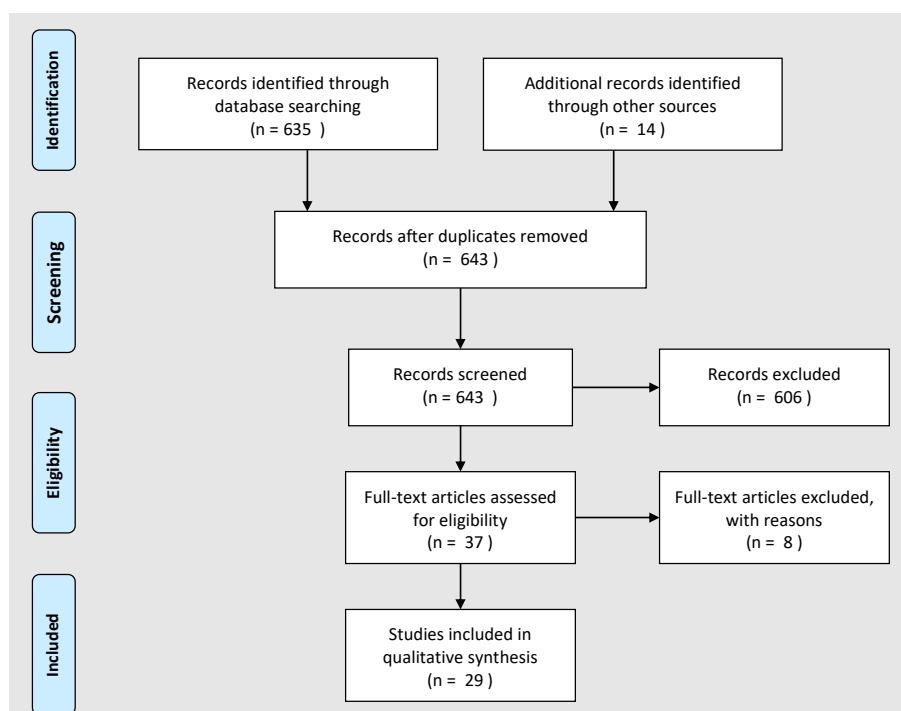


**Figure A1.** Prisma workflow diagram. Out of 643 studies identified, we selected 29 papers for inclusion in the literature review.

The Table below includes the data extracted from the studies included in the review, i.e., the information on the data used in the experiments, methods used for segmentation, and its evaluation results, as well as the QC approaches used for failure detection and the validation results.



Reference	Main Aim Of Paper	Sample size	Patient Population Pathology	Imaging Type	Sequences	Image Segmentation Results	Method	Method	Finding Related To Quality Control	Performance
Brusini, L, Padi	Test QC using a combination of cGANs and CNNs	1600	Healthy and Alzheimer patients	MRI	Not stated	Not stated	Autoencoder networks	CNNs		ROC=0,8
Robinson, R., V	To train a classifier which is able to predict Dice score for segmentation maps	12050	No pathology	CMR	Not stated	The depth of random forest was set to deliberately produce segmentation of good and poor quality. With CNN 99% of segmentation accuracy was achieved.	RF rd CNN	RCA		99% of the segmentation maps were labeled correctly
Valindria, V.V.,	To introduce a classifier which is able to predict Dice score on a per case basis	35	Healthy	MRI	T1w and T2w	Segmentations of varied quality were created	Random Forest, 3D CNNs, and a probabilistic multi-atlas label propagation approach	Single-Atlas, Atlas Forests and Constrained CNNs		Accuracy between 0,6 and 0,88 was achieved
Jungo, A, Balsi	To measure uncertainty of the predictions for the visual QC	285	Cancer	Brain MRI	T1w, T2w, FLAIR	Dice 0,86	Unet	Estimation of uncertainty using MC drop out, Softmax, ensembles, aleatoric uncertainty, auxiliary networks		Ensembles and center+MC shown the highest Dice
Natekar, P., Ko	To extract explanations "uncertainties" for brain tumor segmentation models	285	Cancer	Brain MRI	T1w, T2w, FLAIR, PDw	Dice between 0,74 and 0,83 was achieved	DenseUnet, SimUnet, ResUnet	Network Dissection, Grad-CAM, Activation Maximization, Regularisation, test time dropout		No performance evaluation
Nair, T., Precup	To test various uncertainty measures on the lesion-level predictions and test how filtering based on uncertainty level improves the Dice	2684	Multiple Sclerosis	Brain MRI	T1w, T2w, FLAIR, PDw	At 0,2 FDR operating point, the network has an overall TPR of 0,77	CNN	Predicted variance, entropy, mutual information and MC sample variance		The performance is improved when filtering just 2% of the most uncertain lesions
Wang, G., Li, W	To estimate model and image-based uncertainty on the test-time augmented data	345	Cancer and healthy	Brain and fetus MRI	T1w, T1cw, T2w, FLAIR	Dice between 0,71 and 0,87 was achieved at the baseline	Unet, Wnet, Vnet, FCN, Pnet	TTA-based aleatoric uncertainty, TTD-based epistemic uncertainty		About 2% increase of the Dice score
Zheng, H., Che	To propose a novel approach for model uncertainty estimation	102	Pancreatic Cancer	Pancreas MRI and CT	Not stated	73,88% on cancer MRI dataset and 84,37% on CT scans	Unet	Calculating uncertainty using shadowed sets		Uncertain segmentation method greatly improves performance for pancreas segmentation
Do, H.P., Guo,	To apply deep convolution neural network to the segmentation task in myocardial arterial spin labeled perfusion imaging and to develop methods that measure uncertainty	28	Cardiac	ASL Images	Not stated	U-Net achieved a Dice coefficient of $0,91 \pm 0,04$ on the test set	MCD Unet, prob Unet	MCD uncertainty and Dice uncertainty		Dice uncertainty and Monte Carlo dropout uncertainty were in good agreement ( $R2 = 0,64$ )
Kwon, Y., Won,	To invoke a Bayesian neural network and propose a natural way of quantifying uncertainties in classification problems by decomposing the moment-based predictive uncertainty into two parts: aleatoric and epistemic uncertainty	98	Ischemic stroke and healthy	Brain MRI and Digital Retinal Image	FLAIR, DWI, T1, T2	Not stated	Bayesian neural network	Aleatoric and epistemic uncertainty		Variational predictive uncertainty may not be a good approximation of the predictive uncertainty. However, the epistemic uncertainty can be useful in comparing the variability due to the effective sample size
Kim, Y.C., Kim,	To investigate the usefulness of uncertainty estimation in deep convolutional neural networks for automatic myocardial segmentation	110	Cardiac	Cardiac MRI	Not stated	The mean Dice similarity score of the proposed automatic method was 0,806 ( $\pm 0,096$ )	Unet	MCD uncertainty and SSD score		The SSD metric adopted in this study can be used for screening purposes, so that the cases with high endocardial and epicardial SSD values can be referred for further evaluation and correction by human experts.
Hu, S., Worrall,	To implement a Probabilistic U-Net which outputs aleatoric and epistemic uncertainty for lung nodule and prostate segmentation	1058	Lung and prostate	CT and MRI	Not stated	Generalized energy distance is 0,267	Probabilistic U-Net	Aleatoric and epistemic uncertainty		Predicted $0,669 \pm 0,011$ on CT and $0,345 \pm 0,005$ on MRI data uncertainty
Sander, J., de V	To obtain spatial uncertainty maps with low computational effort using DCNNs	100	Cardiac	CMRI	Not stated	Not stated	Dilated convolutional network	Bayesian DCNNs, entropy, model calibration		(Bayesian) dilated CNN trained with the Brier loss produces valuable Bayesian uncertainty and entropy maps. Our results convey that regions of high uncertainty almost completely cover areas of incorrect segmentations. Well calibrated models enable us to obtain useful spatial entropy maps, which can be used to increase the segmentation performance of the model.
Pan, H., Feng,	To develop a two-stage model which uses a variable-input based uncertainty measure	50	Prostate	MRI	T2	Dice 0,88	Two 3D dilated U-Nets	Bayesian dropout		In terms of uncertainty metrics, the mean probability of foreground pixels was proven to be the most correlated measure with the actual performance, which is reasonable as the label foreground probability can be a good proxy for model's certainty
Norouzi, A., Em	To compute uncertainty of the model output using Monte Carlo sampling in the input space using a well-defined affine transformation	33	Cardiac	MRI	Not stated	Dice 0,88	Unet	Approximate uncertainty (standard deviation)		Dice improved to 0,91
Baumgartner, C	To introduce a novel hierarchical probabilistic method for modelling the conditional distribution of segmentation masks	1086	Thoracic and prostate	CT and MRI	T2	Dice 0.5 for CT thoracic segmentation and 0,8 for MR prostate segmentation	Unet	PHISeg		Increased accuracy
Eaton-Rosen, Z	To utilise a Bayesian deep learning model to measure the uncertainty of image segmentation	285	Cancer	Brain MRI	T1w, T2w, FLAIR	Dice 0,86	Bayesian neural networks	Bayesian neural networks, model calibration		The segmentation method was used also to estimate uncertainty. Dice 0,86
Jungo, A., & Re	To evaluate common uncertainty measures with respect to their reliability, their benefit, and limitations	3015	Cancer, skin lesion	Brain MRI, skin images	T1-weighted, T1-weighted post-contrast, T2-weighted, FLAIR	0,874 Dice on Brats dataset and 0,814 on ISIC	Unet	Softmax entropy, MC dropout, Ensembles, Auxiliary network, model calibration		The highest Dice was achieved with ensembles, 0,879 Dice on Brats dataset and 0,839 on ISIC
Jena, R., & Awk	To propose a novel Bayesian decision theoretic deep-neural network	Not stated	Cancer and healthy	CT and MRI	T1w, T2w, FLAIR	The segmentation method was used also to estimate uncertainty, Dice 0,8	Wnet and Unet	Bayesian DNN, model calibration		Dice 0,804
Kwon, Y., Won,	To implement Bayesian neural networks for uncertainty estimation	58	Ischemic stroke	Brain MRI	TTP, Tmax, CBV, CBF T1c, T2, DWI	The segmentation method was used also to estimate uncertainty, coefficients of Dice or other evaluation metrics were not given	Bayesian neural networks	Bayesian neural networks		The prediction map from the SPES-user-3 partially failed to identify some lesion locations but the uncertainty maps recovered the missed region close to the ground truth.
DeVries, T., & I	To compare different approaches for automatic QC	2750	Skin lesion	Dermoscopic images	Not stated	$0,73 \pm 0,02$ Jaccard index	CNN	Max Probability, MC dropout, HCNN, LCE		All methods shown similar performance apart from the HCNN
Roy, A, G., Cor	To aggregate uncertainty and calibrate predictions	90	Healthy and Alzheimer patients	Brain MRI	T1	$0,806 \pm 0,035$ Dice	QuickNat	MC dropout, scores: coefficient of variation, Dice agreement, intersection over union, mean uncertainty, error bars		Highest correlation of Dice is with intersection over union
Audelan, B., & I	To find more correct segmentation maps and predict Dice	285	Cancer	Brain MRI	T1, T1c, T2 and T2 FLAIR	Not stated	Variational mixtures	Variational mixtures		Correlation between the real Dice and predicted Dice with $R > 0,69$
Liu, F., Xia, Y.,	To learn shape of the region of interest and predict Dice	552	Pancreatic Cancer	Abdominal CT	Not stated	82.15, 57.10 and 66.36 average Dice score on NIH, MSD and Synapse datasets	Bayesian neural networks	VAE, simple linear model		Correlation coefficient between the real and predicted Dice scores ( $R = 0,68$ ) and smaller MAE (0,06)
Xia, Y., Zhang,	To predict error maps and Dice	281	Pancreatic Cancer and healthy	Abdominal CT	Not stated	Not stated	3D AH-Net	GANs, Siamese Neural Network		Correlation of $R=0,61$ as well as 0,18 MAE between predicted Dice and real Dice
Wang, S., Tarrc	To find more correct segmentation maps and predict fake Dice	1600	Cardiac	MRI	Not stated	Not stated	Not stated	VAE, iterative search in latent space, CNN regression		The proposed framework achieved an equivalent performance ( $R=0,96$ , $MAE=0,07$ ) to the regression method ( $R=0,97$ , $MAE=0,06$ )
Zhang, R., & Ci	To predict error maps and quality index	20	Cardiac	MRI	Not stated	Not stated	VoxResNet	GANs		Pearson correlation coefficient between QI and true Dice was 0,85
Zhang, Z., Tian	To predict error maps and accuracy	118	Cardiac, healthy	MRI	Not stated	0,81 Dice	AEP-Net	Encoder-Decoder		Pearson correlation coefficient and MAE between the true segmentation accuracy and quality metric of 0,9873 and 0,0032
Zhou, L., Deng,	To predict error maps and Dice	100	Cardiac	MRI	Not stated	Not stated	Not stated	Reconstruction network, CNN regression		MAE between the predicted and real Dice of 0,12